Article

Efficient Hydrogen Peroxide Generation Utilizing Photocatalytic Oxygen Reduction at a Triphase Interface

$$O_2 + 2e^- + 2H^+ \rightarrow H_2O_2$$

Air   Air

Substrate   Photocatalyst   HS = Hole Scavenger

Zhen Liu, Xia Sheng, Dandan Wang, Xinjian Feng

shengxia@suda.edu.cn (X.S.)
xjfeng@suda.edu.cn (X.F.)

HIGHLIGHTS

A triphase photocatalytic system is developed for efficient H_2O_2 generation

Sufficient interface oxygen is provided

The formation rate is enhanced

The unwanted electron-hole recombination and H_2O_2 decomposition rates are suppressed

Article

Efficient Hydrogen Peroxide Generation Utilizing Photocatalytic Oxygen Reduction at a Triphase Interface

Zhen Liu,[1] Xia Sheng,[1,*] Dandan Wang,[1] and Xinjian Feng[1,2,*]

SUMMARY

Photocatalytic oxygen reduction has garnered attention as an emerging alternative to traditional anthraquinone oxidation process to synthesize H_2O_2. However, despite great efforts to optimize photocatalyst activity, the formation rate has been largely limited by the deficient accessibility of the photocatalysts to sufficient O_2 in water. Here we boost the reaction by reporting an air-liquid-solid triphase photocatalytic system for efficient H_2O_2 generation. The triphase system allows reactant O_2 to reach the reaction interface directly from the ambient atmosphere, greatly increasing the interface O_2 concentration, which in turn simultaneously enhanced the kinetics of formation constant and suppressed the unwanted electron-hole recombination and the kinetics of H_2O_2 decomposition reaction. Compared with a conventional liquid-solid diphase reaction system, the triphase system enables an increase in H_2O_2 formation by a factor of 44. The triphase system is generally applicable to fundamentally understand and maximize the kinetics of semiconductor-based photocatalytic oxygen reduction for H_2O_2 generation.

INTRODUCTION

Hydrogen peroxide (H_2O_2) is a valuable chemical with rapidly growing demand in a wide variety of industrial areas, including fuel cells, chemical oxidation, environment protection, and paper and textile industries (Campos-Martin et al., 2006). The global H_2O_2 market demand is expected to reach 6,000 kilotons in 2024 (www.gminsights.com/pressrelease/hydrogen-peroxide-market). Currently, industrial processes for H_2O_2 synthesis involve the multistep anthraquinone oxidation, which requires complex large-scale infrastructure and large amounts of energy. Thus, developing efficient and cost-effective alternative routes for H_2O_2 generation is of ongoing importance (Edwards et al., 2009; Freakley et al., 2016; Jung et al., 2018; Lu et al., 2018; Siahrostami et al., 2013).

The photocatalytic reduction of oxygen to H_2O_2 has received great attention as it requires only light, water, and O_2 (Baur and Neuweiler, 1927; Cooper and Zika, 1983; Kaynan et al., 2014; Kofuji et al., 2016; Kormann et al., 1988; Liu et al., 2014; Moon et al., 2014; Nakata and Fujishima, 2012; Shiraishi et al., 2014; Sorcar et al., 2018; Teranishi et al., 2010, 2016; Wang et al., 2015). During the reaction photogenerated conduction band (CB) electrons reduce O_2 to produce H_2O_2; $O_2 + 2e^-_{CB} + 2H^+_{aq} \rightarrow H_2O_2$ [(O_2/H_2O_2) = 0.695 V versus normal hydrogen electrode (NHE)]. However, to date resultant product concentrations have been quite limited. The low production rate can be ascribed to the following aspects, which may not be strictly independent of one another: first, the low concentration and slow diffusion rate of O_2 in liquid phase results in deficient accessibility of the photocatalysts to reactant; second, the recombination of electrons and holes limits the electron utilization efficiency, and such limitation becomes more serious in the presence of higher charge carrier concentrations associated with greater light intensities; third, the degradation of H_2O_2 by photogenerated charge carriers also reduces the product yield.

The performance of interfacial catalytic reactions is generally governed by the interface environment. Herein, we simultaneously address these limitations by demonstrating a reaction system possessing an air-liquid-solid triphase reaction interface as illustrated in Figure 1A, where the nanostructured semiconductors are deposited on the top surface of a porous superhydrophobic substrate. Learning from nature, based on the cooperative effect between the low surface energy and rough surface structure, superhydrophobic substrates have been fabricated and used in a wide variety of fields (Aebisher et al., 2013; Deng et al., 2012; Feng et al., 2002; Feng and Jiang, 2006; Hong et al., 2007; Lafuma and Quéré, 2003; Lei

[1]College of Chemistry, Chemical Engineering and Materials Science, Soochow University, Suzhou 215123, P. R. China

[2]Lead Contact

*Correspondence: shengxia@suda.edu.cn (X.S.), xjfeng@suda.edu.cn (X.F.)

https://doi.org/10.1016/j.isci. 2019.06.023
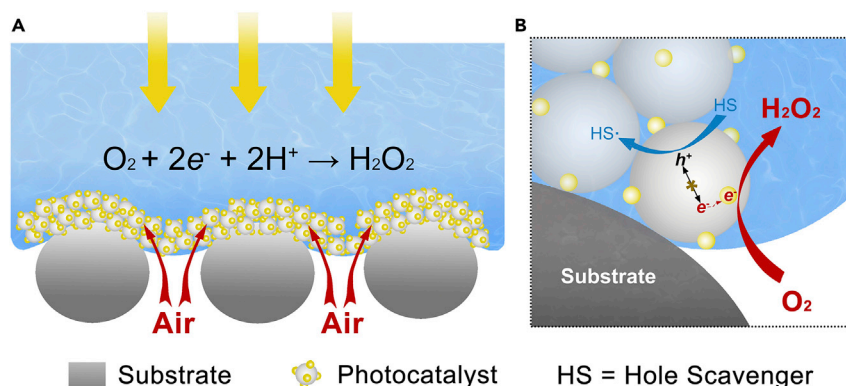
Figure 1. Schematic Illustration of the Triphase Photocatalytic Reaction System

(A) Photocatalysts are immobilized on the porous superhydrophobic substrate.

(B) Enlarged view of the solid-liquid-air triphase reaction zone. Reactant O_2 is rapidly delivered from the air to the reaction interface resulting in a significantly enhanced rate of H_2O_2 production.

et al., 2016; Su et al., 2016; Wooh et al., 2017; Wu et al., 2014; Yohe et al., 2012). When immersed in water the superhydrophobic substrate traps air within atmosphere-linked air pockets, resulting in an interface where solid, liquid, and air three phases coexist (Feng et al., 2002; Lafuma and Quéré, 2003). The triphase system allows reactant O_2 to diffuse directly from the air phase to the reaction interface, rather than by slow diffusion through the liquid. Benefiting from this interface architecture the accessibility of the photocatalyst to O_2 is greatly increased, which in turn (1) enhances the reaction rate between O_2 and photogenerated electrons, (2) suppresses the electron-hole recombination and increases the charge utilization efficiency, and (3) reduces the degradation reaction between H_2O_2 and photogenerated electrons, thus leading to much enhanced rates of H_2O_2 production.

RESULTS AND DISCUSSION

As a proof of concept, we constructed a triphase photocatalytic interface architecture by immobilizing Au-decorated TiO_2 nanoparticles (Au-TiO_2 NPs) (Teranishi et al., 2010) onto a polytetrafluoroethylene-treated superhydrophobic porous membrane composed of carbon fiber (see the "Methods") as shown in Figures 1A and S1 (Supplemental Information). Oxygen can diffuse perpendicularly through the membrane, via air phase, to the reaction interface. Upon UV light illumination the photogenerated electrons transfer from TiO_2 to the Au co-catalyst to react with O_2 via two-electron reaction, in turn producing H_2O_2 (Figure 1B). A structural analysis of the Au-TiO_2/triphase system is shown in Figure 2; the anatase TiO_2 NPs (Figure S2) have an average size of about 200 nm. The hydrophobic carbon fiber substrate has a water contact angle (CA) of 148° (Figure 2A), whereas after photocatalyst deposition (see top of Figure 2A) the surface becomes hydrophilic with a CA of 47°. In such a case, water can wet the hydrophilic photocatalysts but cannot penetrate into the porous hydrophobic substrate, leading to the formation of a triphase reaction interface microenvironment. Imaging by transmission electron microscopy (TEM, high-resolution TEM), see Figure 2C, indicates that the Au NPs are uniformly distributed upon the TiO_2 surface. Fringe spacing of 0.204 and 0.352 nm, respectively, corresponding to the d-spacing of Au (200) and TiO_2 (101) planes, can be observed in Figures 2D and 2E. Figure 2F shows that the average size of the Au NPs is about 5.2 nm.

Photocatalytic synthesis of H_2O_2 was carried out under UV light with a wavelength of 367 ± 5 nm (Figure S3). Control experiments based on a diphase photocatalytic system where the same amount of photocatalyst was dispersed in 1.5 mL water was also conducted. The photocatalytic performances of diphase and triphase reaction systems were first evaluated under UV light of different intensities. Figure S4 shows the H_2O_2 concentration ($[H_2O_2]$) after 1-h reaction under UV light illumination using the triphase reaction system. The reactions initially demonstrate zero-order kinetics, with $[H_2O_2]$ increasing linearly with time. The formation and degradation of H_2O_2 are generally considered to follow, respectively, zero- and first-order kinetics (Kaynan et al., 2014; Kormann et al., 1988; Teranishi et al., 2010). Thus it can be assumed there is negligible H_2O_2 degradation within the first 1 h, allowing the production rate to be calculated as d $[H_2O_2]$/dt. Figure 3A shows the relationship between the calculated H_2O_2 formation rate and light intensities varying between 1 and 120 mW cm^{-2}. Using the triphase system (Figure 3A, red line), the rate of
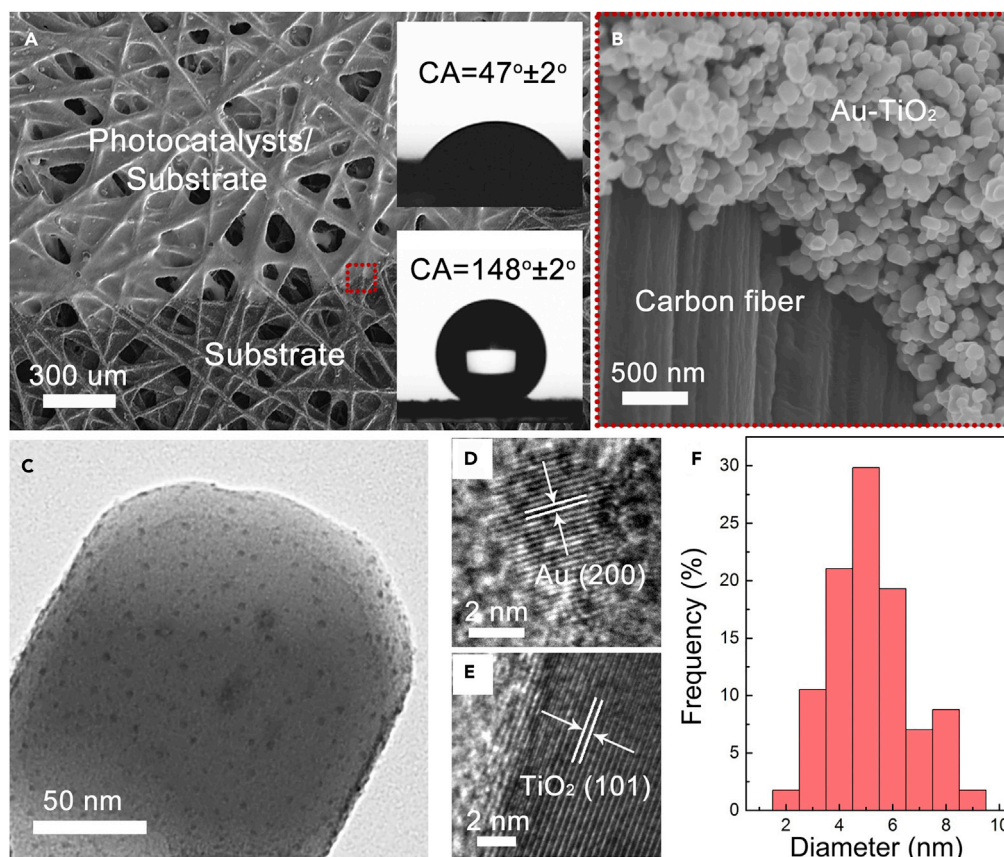
Figure 2. Surface Morphologies and Microstructure Characterizations of the Triphase Reaction System

(A) Scanning electron microscopic (SEM) image of polytetrafluoroethylene-treated superhydrophobic carbon fiber substrate immobilized with Au-TiO$_2$ nanoparticles; inserts are photographs of water droplets placed on the substrate (bottom) and Au-TiO$_2$/substrate (top).

(B) SEM image of the carbon fiber and Au-TiO$_2$ nanoparticles.

(C) TEM image of one individual Au-decorated TiO$_2$ nanoparticle.

(D and E) High-resolution TEM images of (E) TiO$_2$ and (D) Au nanoparticles.

(F) Size distribution of the Au nanoparticles.

production increased with light intensity up to about 60 mW cm^{-2}, whereas in the diphase reaction system (Figure 3A, dark line), the production rate saturates at a light intensity of 3 mW cm^{-2}. The rate of production reaction of the triphase system at a light intensity of 60 mW cm^{-2} was about 18 times faster than that of the diphase reaction system.

The difference in the reaction rates of the diphase and triphase systems can be attributed to their fundamentally different reaction interfacial architectures. With the diphase system O$_2$ is delivered to the photocatalyst surface through the liquid phase with a slow rate of diffusion. Even with air being continuously fed into the solution (Figure S5) the enhancement in H$_2$O$_2$ production with the diphase system is limited (see Figures 3B-I and 3B-II). In contrast, the triphase architecture enables sufficient O$_2$ to be delivered directly from air to the reaction interface. Because the diffusion coefficient of O$_2$ in air (2.0 × 10^{-1} cm^2 s^{-1}) is approximately four orders of magnitude higher than that in water (2.1 × 10^{-5} cm^2 s^{-1}) (Cussler, 1997), O$_2$ consumed at the photocatalyst surface is rapidly resupplied, with O$_2$ concentration in the liquid phase having little impact on the reaction kinetics. As seen in Figure 3B, when O$_2$ levels in water are decreased by feeding the solution with nitrogen (Figure 3B-I) and increased by feeding the solution with air (Figure 3B-iii), the rate of H$_2$O$_2$ formation is essentially unchanged (Figure 3B-ii), indicating that the triphase photocatalytic reaction kinetics is air phase dependent. To confirm that the activity enhancement was due to the enhanced access of the photocatalyst to O$_2$, O$_2$ in the air phase was replaced with N$_2$ as illustrated in Figure S6. The significantly enhanced production rate indicates that rapid mass transport of O$_2$ from air phase
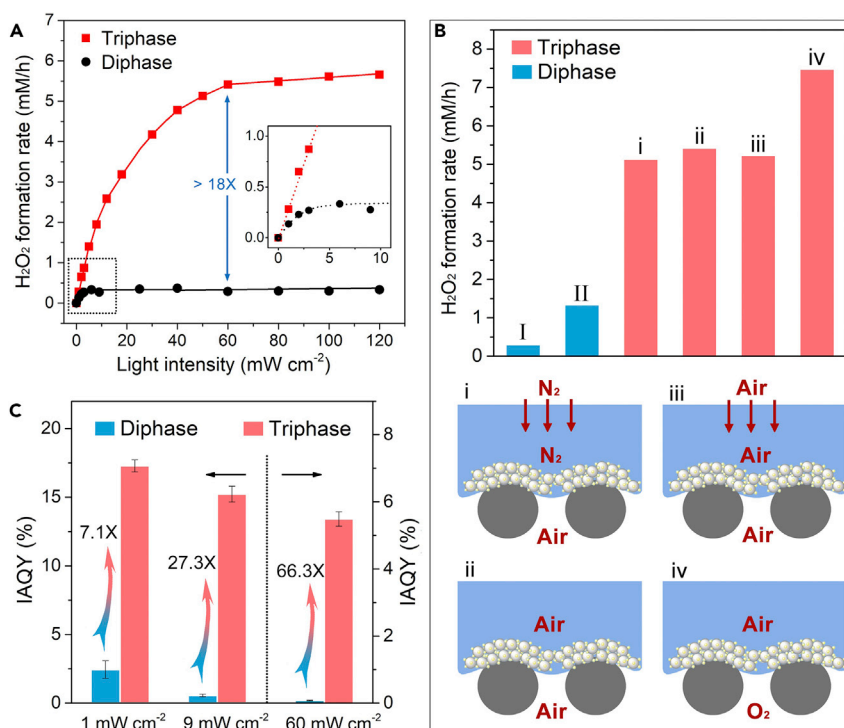
Figure 3. Performance of the Triphase Photocatalytic System for H_2O_2 Generation

(A) Rate of H_2O_2 formation under different light intensities using the triphase (red line) and diphase (dark line) systems.

(B) H_2O_2 formation rates based on different operational conditions using these two systems under illumination of 60 mW cm^{-2}. The bottom panel presents a schematic illustration of the four operational conditions.

(C) IAQYs for the two systems under 1 mW cm^{-2}, 9 mW cm^{-2}, and 60 mW cm^{-2} illumination. Data of IAQYs for 1, 9, and 60 mW cm^{-2} illumination are 17.29 $\pm$ 0.44, 15.23 $\pm$ 0.57, and 5.49 $\pm$ 0.21, respectively, in the triphase system and 2.45 $\pm$ 0.64, 0.55 $\pm$ 0.08, and 0.08 $\pm$ 0.009, respectively, in the diphase system.

to the triphase interface plays a key role in enhancing oxidase kinetics. Increasing interface O_2 partial pressure can further increase the rate of H_2O_2 production; as an example, Figure 3B-iv indicates the effect of replacing air by (pure) oxygen.

The higher O_2 levels at the triphase interface significantly enhance the reaction kinetics between O_2 and electrons, whereas suppressing electron-hole recombination leads, in turn, to higher charge utilization efficiency and quantum yields. The apparent quantum yield (AQY) is defined as the number of electrons used to produce H_2O_2 molecules per unit time to the number of incident photons (Kato et al., 2013). The calculated initial AQY (IAQY) based on triphase system is much higher than that of diphase system over the whole range of light intensities. As shown in Figures 3C and S7, under light intensities of 1 mW cm^{-2}, 9 mW cm^{-2}, and 60 mW cm^{-2}, the IAQYs of the triphase system are, respectively, approximately 7, 27, and 66 times higher than those of the diphase system. From Figure 3C it can also be seen that the IAQY of the diphase system decreases rapidly from 2.45% to 0.55%, a factor of four, as the light intensity is increased from 1 to 9 mW cm^{-2}. The rapid decrease in the IAQY suggests that electron-hole recombination is the dominant process even at modest light intensities. With the triphase system the IAQY decreases only from 17.29% to 15.23% as the light intensity is increased from 1 to 9 mW cm^{-2}, whereas even at 60 mW cm^{-2} the IAQY of the triphase system is still much higher than that of the diphase system at 1 mW cm^{-2}. The effective suppression of electron-hole recombination enables the triphase system to be operated at high light intensities with the large amount of photogenerated electrons efficiently utilized for H_2O_2 production.

The steady-state concentrations (SSC) of H_2O_2 produced using the two interfacial architectures were further investigated. As seen in Figure 4A, an SSC of 26.5 mM was achieved with the triphase system, approximately 44-fold higher than that obtained with the diphase counterpart (0.6 mM). Using our triphase
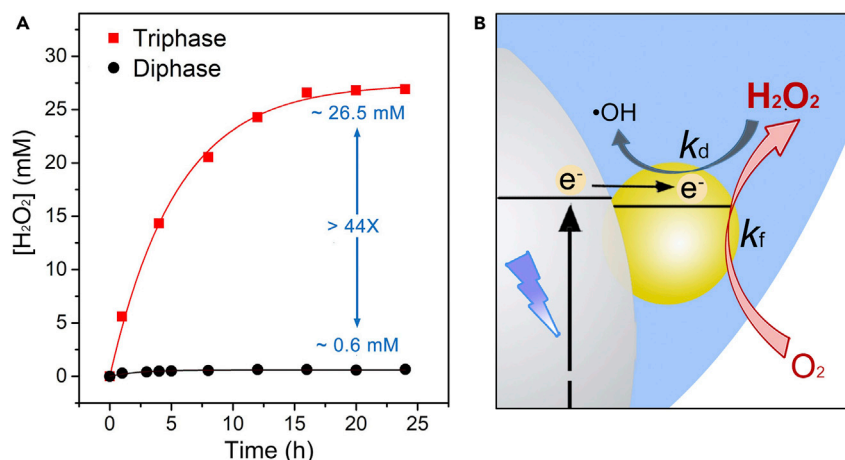
Figure 4. Formation and Degradation Behavior of H$_2$O$_2$

(A) The steady-state concentration of H$_2$O$_2$ produced using the triphase system (red line) and diphase system (dark line) under illumination of 60 mW cm^{-2}.

(B) Schematic illustration of formation and degradation reactions of H$_2$O$_2$ at the triphase interface.

system a steady state H$_2$O$_2$ yield of 59 μmol per unit photocatalyst weight (mg) can be achieved, a value much higher than that of other group reports (Table S1). The SSC of H$_2$O$_2$ depends on the kinetics of both formation and degradation reactions. Generally, the reaction kinetics can be analyzed using the following equation (Kim et al., 2016; Kormann et al., 1988; Teranishi et al., 2010):

$$[H_2O_2] = \left(\frac{k_f}{k_d}\right)\left(1 - \exp(-k_d t)\right)$$

where k_f and k_d are, respectively, the formation and degradation rate constants for H$_2$O$_2$ and t is the reaction time. The [H$_2$O$_2$] formation and degradation reaction rates follow, respectively, zero- and first-order kinetics, where k_f is expressed in mM h^{-1} and k_d in h^{-1}.

As clearly shown in Figure 4A, the experimental data are quite accurately modeled using the equation. The calculated k_f and k_d values of the triphase system are 5.06 mM h^{-1} and 0.18 h^{-1} (Table 1), whereas for the diphase system the k_f and k_d values are 0.26 mM h^{-1} and 0.43 h^{-1}, respectively. We note that for both systems, under 60 mW cm^{-2} illumination, the calculated k_f values are in good agreement with the results from Figure 3A (k_f is equal to the formation rate for zero-order kinetics). With the triphase system not only the k_f was greatly increased but also the k_d was effectively suppressed. As illustrated in Figure 4B the photocatalytic degradation of H$_2$O$_2$ is initiated by its reaction with CB electrons: H$_2$O$_2$ + e$^-_{CB}$ → OH$^-$ + ·OH [(H$_2$O$_2$/·OH) = 0.71 V versus NHE] (Nakata and Fujishima, 2012; Sheng et al., 2014), which competes with the reaction between O$_2$ and electrons (Zhuang et al., 2015). By providing significantly greater amounts of reactant oxygen to the photocatalytic interface, the triphase system suppresses the degradation reaction and enhances the formation reaction, in turn leading to greater H$_2$O$_2$ production.

The stability of the triphase reaction system was further evaluated. We have conducted water breakthrough pressure measurement on Au-TiO$_2$/substrates before and after continuous 24-h UV illumination (60 mM cm^{-2}), in each case achieving a comparable water column height (~89 cm), suggesting a good substrate photostability during photocatalysis of H$_2$O$_2$, of crucial importance to practical applications. The triphase system demonstrated here is applicable to enhance the performance of other photocatalysts. We have studied the activity of photocatalyst ZnFe$_2$O$_4$ (Su et al., 2012) for H$_2$O$_2$ generation. As shown in Figure S8, an SSC of 3.3 mM was achieved based on the triphase system, which is about seven times higher than that of the diphase system under air mass (AM) 1.5 simulated sunlight. This result indicates that the triphase system provides an exploratory platform, on which different kinds of photocatalysts can be applied for efficient H$_2$O$_2$ generation.

In conclusion, we have constructed a photocatalytic system with a triphase solid-liquid-air reaction interface for efficient H$_2$O$_2$ synthesis. The triphase interface allows reactant O$_2$ to be rapidly delivered to

	k_f (mM h^{-1})	k_d (h^{-1})	k_f/k_d (mM)
Triphase System	5.06	0.18	28.11
Diphase System	0.26	0.43	0.60

Table 1. Calculated k_f, k_d, and k_f/k_d Values of Triphase System and Diphase System

the photocatalyst surface, greatly enhancing the formation reaction and reducing the degradation reaction. The rapid accessibility of O_2 to the photocatalyst surface effectively suppresses electron-hole recombination, enabling the triphase system to efficiently utilize the larger amounts of electrons obtained at higher light intensities to, in turn, produce more H_2O_2. Our results reveal that rational interface micro-environment (wettability and architecture) design is crucial for achieving efficient photocatalytic reaction system for H_2O_2 generation. The triphase reaction system is general; for practical applications, photocatalysts of much lower cost could presumably be used for efficient synthesis of the desired products.

Limitations of the Study

The Au NPs play a vital role in H_2O_2 generation. In this article, the size and density of Au NPs was not adjusted. In our future work, we will adjust the amount and the size of Au to further optimize the H_2O_2 photocatalytic synthesis.

METHODS

All methods can be found in the accompanying Transparent Methods supplemental file.

SUPPLEMENTAL INFORMATION

Supplemental Information can be found online at https://doi.org/10.1016/j.isci.2019.06.023.

AUTHOR CONTRIBUTIONS

Z.L. carried out the experiments. D.W. performed the SEM analysis and TEM analysis. X.S. wrote the paper. X.F. supervised the project and revised the paper.

DECLARATION OF INTERESTS

The authors declare no competing interests.

REFERENCES

Aebisher, D., Bartusik, D., Liu, Y., Zhao, Y., Barahman, M., Xu, Q., Lyons, A.M., and Greer, A. (2013). Superhydrophobic photosensitizers. mechanistic studies of $^1O_2$ generation in the plastron and solid/liquid droplet interface. J. Am. Chem. Soc. *135*, 18990–18998.

Baur, E., and Neuweiler, C. (1927). Über photolytische bildung von hydroperoxyd. Helv. Chim. Acta *10*, 901–907.

Campos-Martin, J.M., Blanco-Brieva, G., and Fierro, J.L.G. (2006). Hydrogen peroxide

synthesis: an outlook beyond the anthraquinone process. Angew. Chem. Int. Ed. *45*, 6962–6984.

Cooper, W.J., and Zika, R.G. (1983). Photochemical formation of hydrogen peroxide in surface and ground waters exposed to sunlight. Science *220*, 711–712.

Cussler, E. (1997). Diffusion: Mass Transfer in Fluid Systems, Second Edition (Cambridge University Press).

Deng, X., Mammen, L., Butt, H.-J., and Vollmer, D. (2012). Candle soot as a template for a

transparent robust superamphiphobic coating. Science *335*, 67–70.

Edwards, J.K., Solsona, B., N, E.N., Carley, A.F., Herzing, A.A., Kiely, C.J., and Hutchings, G.J. (2009). Switching off hydrogen peroxide hydrogenation in the direct synthesis process. Science *323*, 1037–1041.

Feng, X.J., and Jiang, L. (2006). Design and creation of superwetting/antiwetting surfaces. Adv. Mater. *18*, 3063–3078.

Feng, L., Li, S., Li, Y., Li, H., Zhang, L., Zhai, J., Song, Y., Liu, B., Jiang, L., and Zhu, D. (2002). Super-hydrophobic surfaces: from natural to artificial. Adv. Mater. 14, 1857–1860.

Freakley, S.J., He, Q., Harrhy, J.H., Lu, L., Crole, D.A., Morgan, D.J., Ntainjua, E.N., Edwards, J.K., Carley, A.F., Borisevich, A.Y., et al. (2016). Palladium-tin catalysts for the direct synthesis of H_2O_2 with high selectivity. Science 351, 965–968.

Hong, X., Gao, X., and Jiang, L. (2007). Application of superhydrophobic surface with high adhesive force in no lost transport of superparamagnetic microdroplet. J. Am. Chem. Soc. 129, 1478–1479.

Jung, O., Pegis, M.L., Wang, Z., Banerjee, G., Nemes, C.T., Hoffeditz, W.L., Hupp, J.T., Schmuttenmaer, C.A., Brudvig, G.W., and Mayer, J.M. (2018). Highly active NiO photocathodes for H_2O_2 production enabled via outer-sphere electron transfer. J. Am. Chem. Soc. 140, 4079–4084.

Kato, S., Jung, J., Suenobu, T., and Fukuzumi, S. (2013). Production of hydrogen peroxide as a sustainable solar fuel from water and dioxygen. Energy Environ. Sci. 6, 3756–3764.

Kaynan, N., Berke, B.A., Hazut, O., and Yerushalmi, R. (2014). Sustainable photocatalytic production of hydrogen peroxide from water and molecular oxygen. J. Mater. Chem. A 2, 13822–13826.

Kim, H.-i., Kwon, O.S., Kim, S., Choi, W., and Kim, J.-H. (2016). Harnessing low energy photons (635 nm) for the production of H_2O_2 using upconversion nanohybrid photocatalysts. Energy Environ. Sci. 9, 1063–1073.

Kofuji, Y., Ohkita, S., Shiraishi, Y., Sakamoto, H., Tanaka, S., Ichikawa, S., and Hirai, T. (2016). Graphitic carbon nitride doped with biphenyl diimide: efficient photocatalyst for hydrogen peroxide production from water and molecular oxygen by sunlight. ACS Catal. 6, 7021–7029.

Kormann, C., Bahnemann, D.W., and Hoffmann, M.R. (1988). Photocatalytic production of hydrogen peroxides and organic peroxides in aqueous suspensions of titanium dioxide, zinc

oxide, and desert sand. Environ. Sci. Technol. 22, 798–806.

Lafuma, A., and Quéré, D. (2003). Superhydrophobic states. Nat. Mater. 2, 457–460.

Lei, Y., Sun, R., Zhang, X., Feng, X., and Jiang, L. (2016). Oxygen-rich enzyme biosensor based on superhydrophobic electrode. Adv. Mater. 28, 1477–1481.

Liu, X., Xu, H., Grabstanowicz, L.R., Gao, S., Lou, Z., Wang, W., Huang, B., Dai, Y., and Xu, T. (2014). Ti^{3+} self-doped TiO_{2-x} anatase nanoparticles via oxidation of TiH_2 in H_2O_2. Catal. Today 225, 80–89.

Lu, Z., Chen, G., Siahrostami, S., Chen, Z., Liu, K., Xie, J., Liao, L., Wu, T., Lin, D., Liu, Y., et al. (2018). High-efficiency oxygen reduction to hydrogen peroxide catalysed by oxidized carbon materials. Nat. Catal. 1, 156–162.

Moon, G.-h., Kim, W., Bokare, A.D., Sung, N.-e., and Choi, W. (2014). Solar production of H_2O_2 on reduced graphene oxide–TiO_2 hybrid photocatalysts consisting of earth-abundant elements only. Energy Environ. Sci. 7, 4023–4028.

Nakata, K., and Fujishima, A. (2012). TiO_2 photocatalysis: design and applications. J. Photochem. Photobiol. C 13, 169–189.

Sheng, J., Li, X., and Xu, Y. (2014). Generation of H_2O_2 and OH radicals on Bi_2WO_6 for phenol degradation under visible light. ACS Catal. 4, 732–737.

Shiraishi, Y., Kanazawa, S., Kofuji, Y., Sakamoto, H., Ichikawa, S., Tanaka, S., and Hirai, T. (2014). Sunlight-driven hydrogen peroxide production from water and molecular oxygen by metal-free photocatalysts. Angew. Chem. Int. Ed. 53, 13454–13459.

Siahrostami, S., Verdaguer-Casadevall, A., Karamad, M., Deiana, D., Malacrida, P., Wickman, B., Escudero-Escribano, M., Paoli, E.A., Frydendal, R., Hansen, T.W., et al. (2013). Enabling direct H_2O_2 production through rational electrocatalyst design. Nat. Mater. 12, 1137–1143.

Sorcar, S., Thompson, J., Hwang, Y., Park, Y.H., Majima, T., Grimes, C.A., Durrant, J.R., and In, S.-I. (2018). High-rate solar-light photoconversion of CO_2 to fuel: controllable transformation from C1 to C2 products. Energy Environ. Sci. 11, 3183–3193.

Su, L., Feng, J., Zhou, X., Ren, C., Li, H., and Chen, X. (2012). Colorimetric detection of urine glucose based $ZnFe_2O_4$ magnetic nanoparticles. Anal. Chem. 84, 5753–5758.

Su, B., Tian, Y., and Jiang, L. (2016). Bioinspired interfaces with superwettability: from materials to chemistry. J. Am. Chem. Soc. 138, 1727–1748.

Teranishi, M., Naya, S.-i., and Tada, H. (2010). In situ liquid phase synthesis of hydrogen peroxide from molecular oxygen using gold Nanoparticle-Loaded Titanium(IV) dioxide photocatalyst. J. Am. Chem. Soc. 132, 7850–7851.

Teranishi, M., Hoshino, R., Naya, S.-i., and Tada, H. (2016). Gold-nanoparticle-loaded carbonate-modified titanium(IV) oxide surface: visible-light-driven formation of hydrogen peroxide from oxygen. Angew. Chem. Int. Ed. 55, 12773–12777.

Wang, C., Zhang, X., and Liu, Y. (2015). Promotion of multi-electron transfer for enhanced photocatalysis: a review focused on oxygen reduction reaction. Appl. Surf. Sci. 358, 28–45.

Wooh, S., Encinas, N., Vollmer, D., and Butt, H.-J. (2017). Stable hydrophobic metal-oxide photocatalysts via grafting polydimethylsiloxane brush. Adv. Mater. 29, 1604637.

Wu, Y., Liu, K., Su, B., and Jiang, L. (2014). Superhydrophobicity-mediated electrochemical reaction along the solid–liquid–gas triphase interface: edge-growth of gold architectures. Adv. Mater. 26, 1124–1128.

Yohe, S.T., Colson, Y.L., and Grinstaff, M.W. (2012). Superhydrophobic materials for tunable drug release: using displacement of air to control delivery rates. J. Am. Chem. Soc. 134, 2016–2019.

Zhuang, H., Yang, L., Xu, J., Li, F., Zhang, Z., Lin, H., Long, J., and Wang, X. (2015). Robust photocatalytic H_2O_2 production by octahedral $Cd_3(C_3N_3S_3)_2$ coordination polymer under visible light. Sci. Rep. 5, 16947.

Supplemental Information

Efficient Hydrogen Peroxide Generation

Utilizing Photocatalytic Oxygen Reduction

at a Triphase Interface

Zhen Liu, Xia Sheng, Dandan Wang, and Xinjian Feng

Supplementary Information
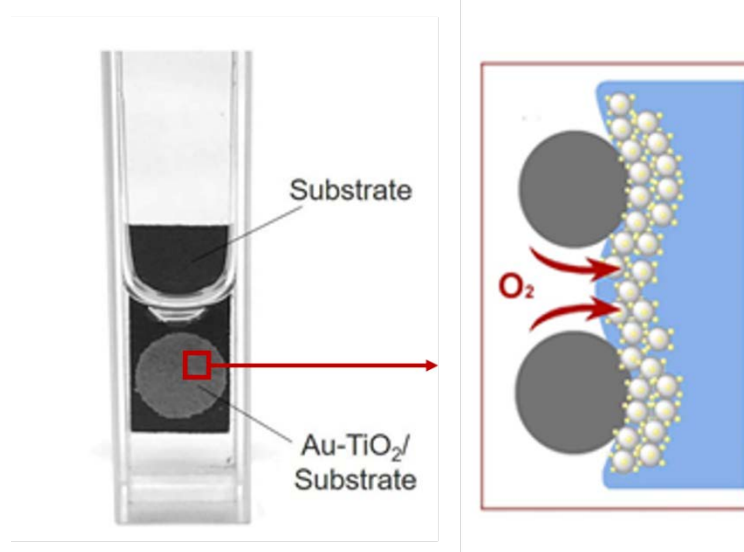
Figure S1. Experimental setup for photocatalytic synthesis of H_2O_2 using the triphase reaction system, related to Figure 1a. Because the backside of the porous membrane is superhydrophobic, it can trap atmosphere linked air phase. Consequently, oxygen can thus diffuse through the membrane, from the via air phase, to the reaction interface.
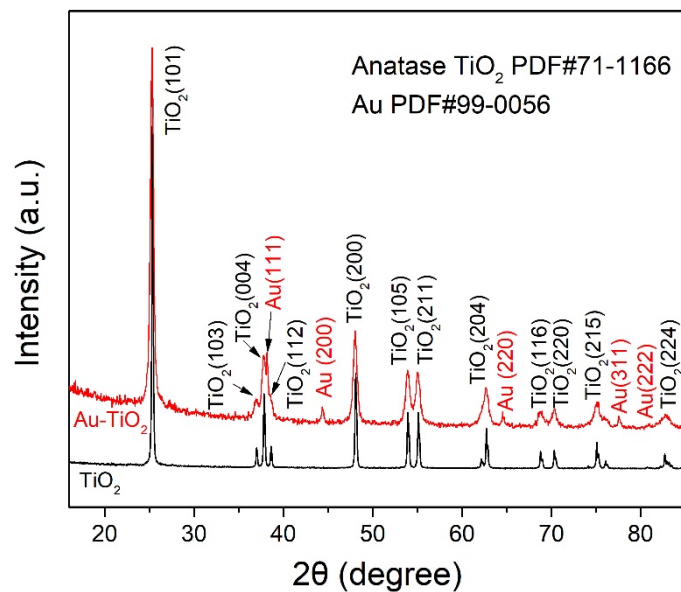
Figure S2. XRD patterns of TiO₂ with and without Au nanoparticles, related to Figure 2a. The standard PDF card numbers for Au and TiO₂ are given in the inset of the Figure. The peak position of Au (111) (38.18°) is very close to that of TiO₂ (112) peak (38.57°). Besides that, the peaks of Au (200), Au (220), Au (311) and Au (222) can be easily seen and well fitted with the standard PDF card, indicating the presence of Au on the catalyst.
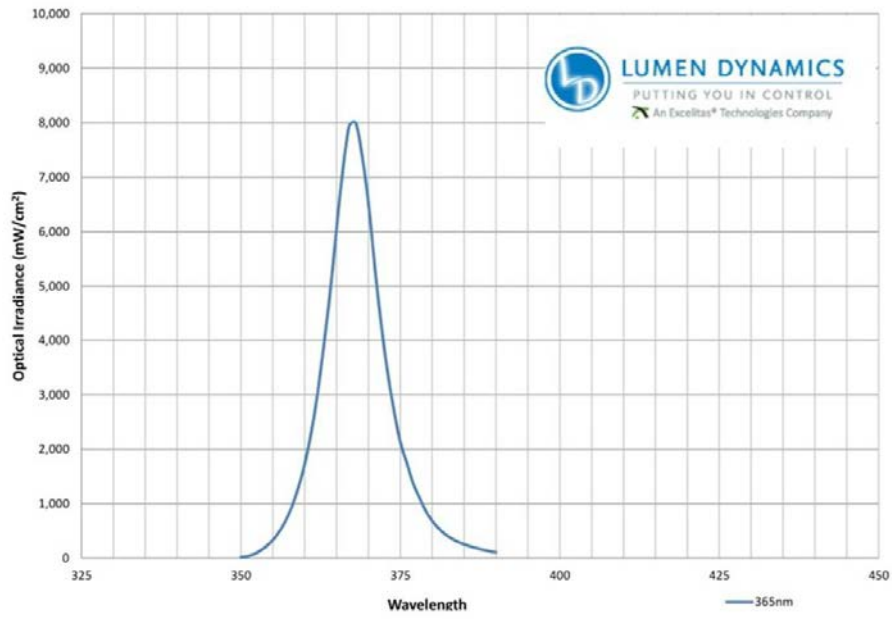
Figure S3. Emission spectrum of the UV lamp used in the experiments, related to Figure 3a.
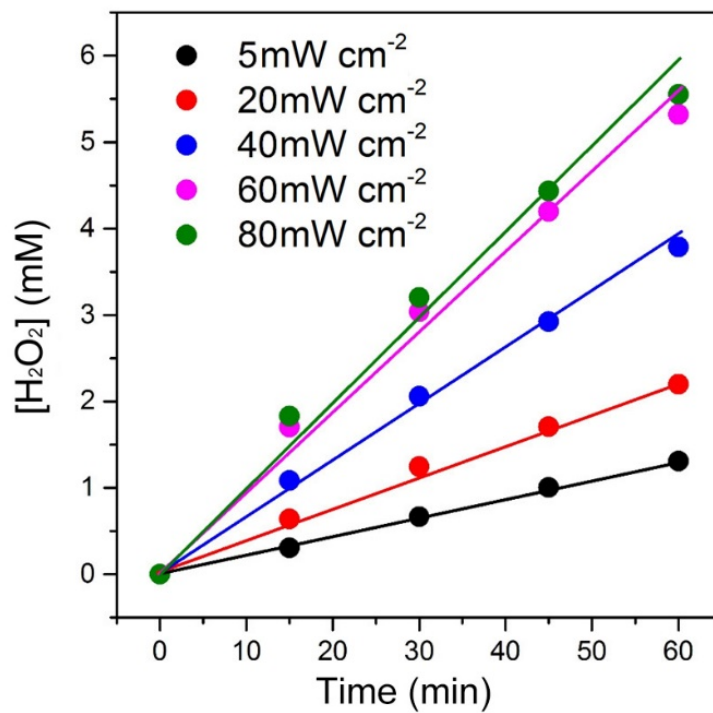
Figure S4. Using the triphase system, H_2O_2 concentration as a function of reaction time under different UV light intensities. Related to Figure 3a.
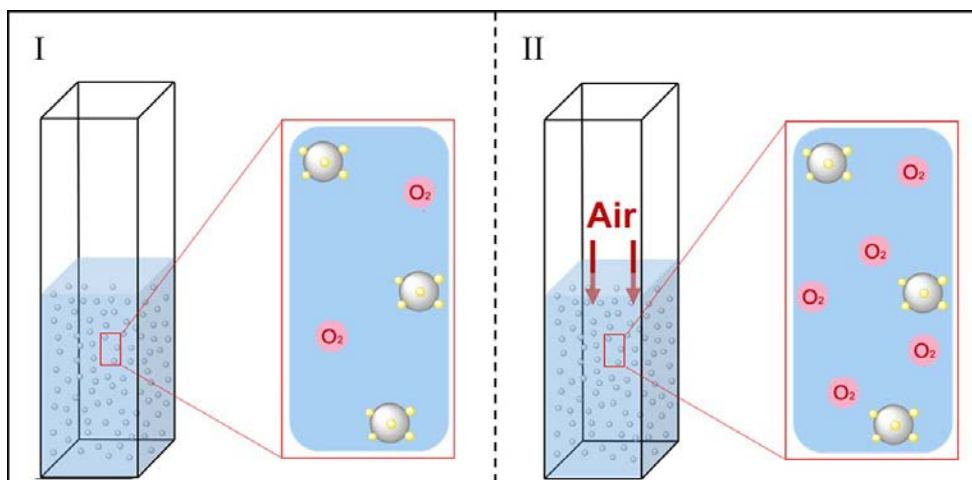
Figure S5. Schematic illustration of the two diphase operational conditions, related to Figure 3b.
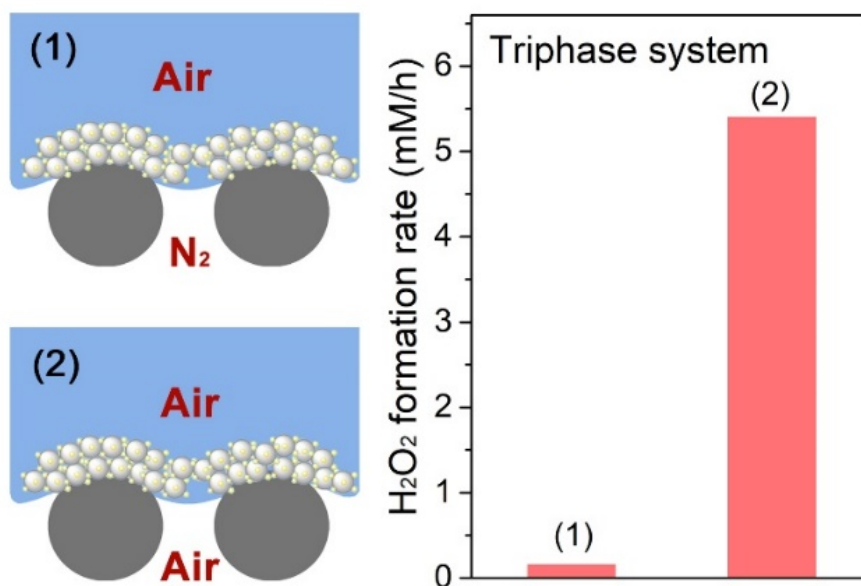
Figure S6. Schematic illustration and H_2O_2 production rate of triphase reaction system when operated in: air (2), and nitrogen (1) atmospheres, related to Figure 3b.The significantly enhanced production rate observed in air indicates that rapid mass transport of O_2 from air phase to the triphase interface plays a key role in enhancing oxidase kinetics.
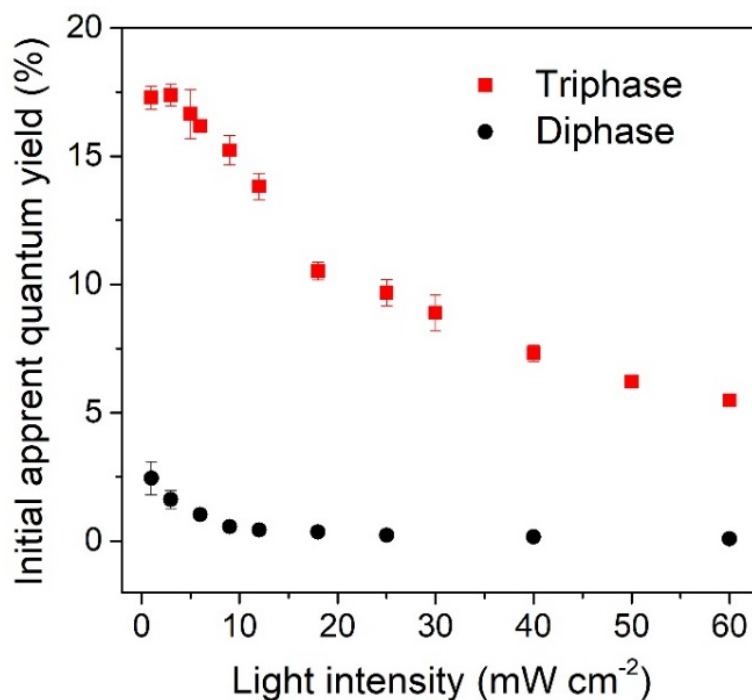
Figure S7. Initial (1 h) apparent quantum yield (AQY) under different UV light intensities for the triphase system (red squares) and diphase system (black circles), related to Figure 3c. The AQY is defined as the number of electrons used to produce H_2O_2 per unit time to the number of incident photons, which represents the utilization efficiency of the photogenerated electrons. The AQY values of triphase system are much higher than that of diphase system over the whole range of light intensities, indicating the electrons utilization efficiency is much higher in triphase system. Despite the AQY values decrease in both systems with the increase in light intensity, their decreasing speeds are different. Under low light intensity, such as 1 mW cm^{-2}, the AQY values of these two systems has about 7-ford difference, whereas, under high light intensity, such as 60 mW cm^{-2}, the AQY value of triphase system is over 62-ford higher than that of diphase system. Based on the triphase system, the fast delivery of O_2 improves the electron utilization efficiency and the photocatalytic reaction kinetics.
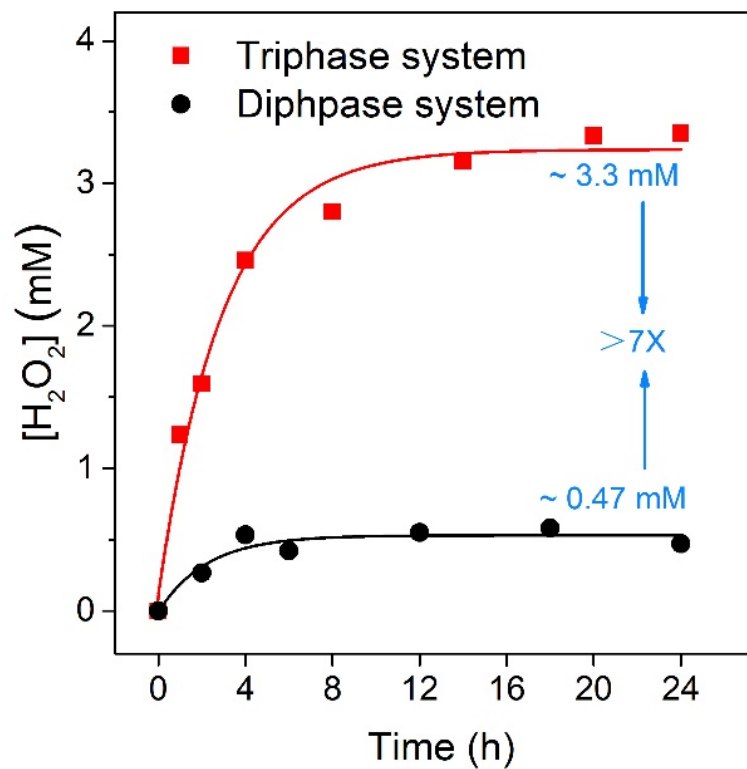
Figure S8. The steady state concentration of H_2O_2 produced using a visible light response photocatalyst $ZnFe_2O_4$ based on the triphase system (red line) and diphase system (dark line) under AM 1.5, related to Figure 4.

Table S1. Comparison of the performance between triphase reaction system and previous reports about photocatalytic H_2O_2 generation, related to Figure 4a

Photocatalyst	Light	Atmosphere	Yield (μmol/mg)	Initial rate (μmol/mg • h)	Reference
Au-BiVO$_4$	$\lambda > 420$ nm	O$_2$, 1 atm	0.024 (10 h)	0.009	*ACS Catal.* 2016, 6, 4976.
g-C$_3$N$_4$/PDI$_{51}$	$\lambda > 420$ nm	O$_2$, 1 atm	0.0306 (48 h)	/	*Angew. Chem. Int. Ed.* 2014, 53, 13454.
g-C$_3$N$_4$	$\lambda > 420$ nm	O$_2$, 1 atm	1.5 (12 h)	/	*ACS Catal.* 2014, 4, 774.
GCN	$\lambda > 420$ nm	O$_2$, 1 atm	4.5 (24 h)	0.19	*ACS Catal.* 2015, 5, 3058.
KPD (K$_2$HPO$_4$) -CN	$\lambda > 420$ nm	O$_2$ Saturated	6 (12 h)	0.5	*ACS Catal.* 2017, 7, 2886.
CdS-SNC/GOND	$\lambda = 635$ nm	O$_2$ Saturated	0.2 (1 h)	0.2	*Energy Environ. Sci.* 2016, 9, 1063.
Au-TiO$_2$	$\lambda > 430$ nm	/	1 (1 h)	1	*Angew. Chem. Int. Ed.* 2016, 55, 12773.
Pd/APTMS/TiO$_2$	Sunlight (AM 1.5)	O$_2$, 1 atm	1.2 (4 h)	0.375	*ACS Catal.* 2019, 9, 626.
ZnFe$_2$O$_4$	Sunlight (AM 1.5)		6.3 (8 h)	2.7	***This work*** (Triphase system)
TiO$_2$	$\lambda > 280$ nm	O$_2$, 1 atm	4 (12 h)	/	*ACS Catal.* 2013, 3, 2222.
Ag/TiO$_2$-P	$\lambda > 320$ nm	O$_2$ Saturated	12 (3 h)	6	*Energy Environ. Sci.* 2014, 7, 4023.
Au$_{0.1}$Ag$_{0.4}$/TiO$_2$	$\lambda > 280$ nm	O$_2$, 1 atm	3.4 (12 h)	0.5	*ACS Catal.* 2012, 2, 599.
Au-TiO$_2$	$\lambda > 300$ nm	/	14 (24 h)	1.8	*J. Am. Chem. Soc.* 2010, 132, 7850.
F-TiO$_2$	$\lambda = 360$ nm	Air Saturated	12 (2 h)	8.4	*Chem. Commun.* 2005, 2627.
Au-TiO$_2$	$\lambda = 367$ nm		59 (16 h)	12.3	***This work*** (Triphase system)

Initial rate (μmol/mg·h) is calculated when [H_2O_2] increases linearly with time.

TRANSPARENT METHODS

Photocatalyst preparation and immobilization:

Au particles were loaded on TiO_2 particles with a crystal form of anatase and a specific surface area of 8.1 $m^2 g^{-1}$ (A-100, Ishihara Sangyo) by the deposition precipitation method[10] using $HAuCl_4$ as a starting material. The pH of 4.86 mM aqueous solution (100 mL) of $HAuCl_4$ was neutralized by NaOH (1 M) to 6.0, and 10 g of the TiO_2 particles were added to the solution. The resulting suspension was stirred at 343 K for 1 h. The particles were washed with distilled water three times and dried under vacuum. Then the post-heating was carried out at 873 K for 20 h to obtain Au/TiO_2. To preclude the influence of the crystallinity, change on the photocatalytic activity of TiO_2, all the TiO_2 particles were used as a support of Au particles after heating 923 K for 4 h. Photocatalyst $ZnFe_2O_4$ nanoparticles was prepared according to a previous report. (Su et al., 2012)

Polytetrafluoroethylene (PTFE) treated porous membrane composed of carbon fibers was used as substrate to immobilize the TiO_2 nanoparticles. One side of the PTFE-treated porous membrane was rinsed by short-term O_2 plasma prior to the photocatalyst immobilization. An Au/TiO_2 or $ZnFe_2O_4$ suspension (5 g L^{-1}) was ultrasonic processed for 4 min, then immobilized on the substrate surface by dripping a 0.134 mL suspension forming an area about 0.5 cm^2 and dried at 353 K for 30 min. Finally, the photocatalyst-immobilized substrate was heated in a box-furnace at 673 K for 1 h then allowed to cool to room temperature.

Characterization

Morphologies were observed by scanning electron microscopy (SEM, HitachiS4800, Japan) and transmission electron microscopy (TEM, Tecnai G2 F20 S-Twin, America). The structure and crystallization of the particles were characterized by X-ray diffraction (XRD, Bruker AXSD8 Advance, Germany). Oxygen plasma treatment was performed using a plasma cleaner (Ming Heng, PDC-MG, China). Photocatalytic degradation was measured by a UV-Vis spectrophotometer (EVOLUTION 220, Thermo, America).

Photocatalytic H_2O_2 synthesis

The photocatalytic reactions using $Au-TiO_2$ were conducted in a quartz cell (1.0 cm × 1.0 cm × 4.5 cm) containing a mixed solutions of 1.5 mL aqueous solution (4% EtOH and 0.1 M NaF) and 0.175 mL PBS solution (pH=3). The portion of substrate that immobilized with TiO_2 was immersed in solution, while another part of substrate (without photocatalysts) was exposed to air. Oxygen can

thus diffuse through the membrane, via air phase, to the reaction interface. Control experiments based on a diphase photocatalytic system where the same amount of photocatalyst was dispersed in water was also conducted. The photocatalytic system was then irradiated with a UV lamp at a wavelength of 367 ± 5 nm with different light intensities. The photocatalytic reaction using $ZnFe_2O_4$ was carried in a quartz cell (1.0 cm $\times$ 1.0 cm $\times$ 4.5 cm) containing 1.5 mL aqueous solution of 4% formic acid under AM 1.5 simulated sunlight. The diphase reaction system was fabricated by immobilizing the same amount of $ZnFe_2O_4$ photocatalysts on a ground glass substrate. Magnetic stirring of the suspension was continued throughout illumination. The temperature of the quartz cell was kept at 298 K. The concentrations of generated H_2O_2 were determined by iodometric titration using the UV-Vis spectrophotometer.

Reference

Su, L., Feng J., Zhou X., Ren C., Li H., and Chen X. (2012) Colorimetric Detection of Urine Glucose Based $ZnFe_2O_4$ Magnetic Nanoparticles. Anal. Chem. *84*, 5753-5758.